Title
Velocity Contrast across the Zhaotong-Ludian Fault in Southwest China from the Analysis of Fault Zone Head Waves and Teleseismic P -Wave Arrivals

Journal
Seismological Research Letters, 93(5)

ISSN
0895-0695

Authors
Zheng, Xian
Zhao, Cuiping
Qiu, Hongrui
et al.

Publication Date
2022-09-01

DOI
10.1785/0220210358

Peer reviewed

Velocity Contrast across the Zhaotong-Ludian Fault in SW China from the analysis of Fault Zone Head Waves and Teleseismic P-Wave Arrivals

Xian Zheng[1], Cuiping Zhao[1*], Hongrui Qiu[2,3], Fenglin Niu[2,4], Ce Zhao[5]

1. Institute of Earthquake Forecasting, China Earthquake Administration, Beijing, 100036, China

2. Department of Earth, Environmental and Planetary Sciences, Rice Universitys, Houston, TX77005, USA

3. Earth, Atmospheric and Planetary Sciences, Massachusetts Institute of Technology, Cambridge, MA02139, USA

4. State Key Laboratory of Petroleum Resources and Prospecting and Unconventional Petroleum Research Institute, China University of Petroleum at Beijing, Beijing 102249, China

5. Institute of Geophysics, China Earthquake Administration, Beijing, 100081, China

*Corresponding author: zhaocp@ief.ac.cn

Declaration of Competing Interests

The authors acknowledge there are no conflicts of interest recorded.

Abstract

We image the Zhaotong-Ludian fault (ZLF) in the southeastern margin of Tibetan Plateau (SE Tibetan Plateau) using waveforms from local and teleseismic earthquakes recorded by 14 seismic stations. We identify two types of fault zone head wave (FZHW) from two clusters of earthquakes by applying an automatic picking algorithm and a horizontal particle motion analysis. The first type of FZHWs shows a linear time-distance moveout and is only observed at stations in southeast side of the fault in the northeastern (NE) section of ZLF. The moveout slope suggests an average cross-fault velocity contrast of ~2.5%. The second type FZHWs exhibits a constant moveout and is recorded by stations on both sides of ZLF in the southwestern (SW) section from a cluster of earthquakes located in a low velocity zone. The difference in cross-fault velocity contrast between the NE and SE segments of the ZLF is also confirmed by teleseismic P-wave traveltime data. We attribute the prominent velocity contrast in the NE section to lithological difference between the South China block in the southeast and the Daliangshan sub-block in the northwest side of the fault. The striking difference between the NE and SW sections also implies that earthquakes nucleating in one segment would hardly rupture through the entire fault, which can significantly affect our estimates of the maximum magnitude of future earthquakes occurring on the fault.

Introduction

The northeast striking Zhaotong-Ludian fault (ZLF) and Lianfeng fault (LFF) are a part of the boundary that separates the active and deformed Daliangshan sub-block (DLSB) in the northwest and the stable South China block (SCB) in the southeast (Figure 1 bottom-right inset). The two faults show a right lateral motion coupled with a reverse slip component (Wen et al., 2013; Chang et al., 2014). The ZLF is a complicated fault system, composed of the main branch and two NE striking secondary faults, the Sayuhe fault (SYHF) and the Longshu fault (LSF) (Chang et al., 2014; Figure 1).

Wen et al. (2013) suggested that the ZLF can produce a M_w 7.4 earthquake based on the magnitude-rupture area empirical formula (Wells and Coppersmith 1994; Leonard 2010) and the assumption of considering seismicity gap as the maximum rupture area. On August 3, 2014, a M_w 6.1 earthquake occurred in the Ludian County at the intersection of the ZLF and the NW striking Baogunao-Xiaohe secondary Fault (BXF) with a focal depth of ~12 km (Figure 1). The BXF also divides the ZLF into a northeastern (NE) and a southwestern (SW) segment, which exhibit very different deformation rates based on GPS data. The M_w 6.1 Ludian earthquake likely only releases part of the accumulated strain in this area, as indicated by the coseismic displacements from GPS observations and inversion analysis, implying that ZLF is still a high-risk region and has a potential to host an even stronger earthquake in the future (Wei et al. 2018).

While plenty of regional-scale body wave tomography studies have been conducted across the SE Tibetan Plateau, which has a relatively good coverage of seismic networks (Guo et al. 2009； Wang et al. 2010; Yang et al. 2014; Xu et al. 2015; Huang et al. 2018), the crustal structures surrounding ZLF were poorly studied before the 2014 M_w 6.1 Ludian earthquake, due to sparse station coverage. After the Ludian earthquake, a temporary seismic network was installed around the ZLF due to the potential risk of a strong earthquake on the ZLF. Wang et al. (2015) inverted crustal structure beneath the ZLF and its surrounding region using teleseismic arrivals recorded by 35 temporary stations deployed around ZLF. Riaz et al. (2017) inverted for P-wave velocity around ZLF using 87 temporary and permanent stations and found a low *Vp* in the source region of the earthquake. Li et al. (2019) took advantage of both the permanent stations from the regional digital seismic networks in SE Tibet and the temporary stations of the ChinArray project and constructed a *P*-wave velocity model with a lateral resolution of 0.5° × 0.5° for an area surrounding the Zhaotong and Lianfeng fault zones. However, due to the limitations of seismic network coverage and sensitivity of P-wave traveltimes, the internal fine structures of ZLF in the upper crust are still yet to be resolved.

Analysis of high-resolution fault zone structure (e.g., velocity contrast across fault, low-velocity damage zone) complements existing regional-scale tomography models, and thus is of great significance to the perception of the seismic generation, occurrence, and rupture (e.g., Qiu et al. 2021). For example, unilateral rupture is expected to occur along bi-material faults (Ampuero and Ben-Zion 2008; Andrews and Ben-Zion 1997; Shlomai and Fineberg, 2016; Weertman 1980). Fault zone head waves (FZHWs), which propagate along a bi-material fault interface along the fast-velocity side and then refract to the slow side (Allam et al., 2014. Figure 3), were first observed and studied by Ben-Zion and Marlin (1991). Since most of the propagation path of FZHW is along the fault interface, the detection of FZHW provides direct evidence for a bi-material fault interface with a velocity contrast. Ross and Ben-Zion (2014) developed an automatic algorithm to distinguish the emergent FZHWs from direct P waves using only the vertical component recording of a single station. However, the automatic algorithm exhibits a high false detection rate as it uses only vertical component data. Later studies (e.g., Share et al. 2016, 2018;

Qiu et al. 2017, 2021) indicated that most of the false detections can be eliminated through a horizontal particle motion analysis (Bulut et al. 2012).

The analysis of FZHWs, such as the distribution of stations with FZHW detections, and differential time between FZHW and P-wave as a function of source-receiver locations, provides high-resolution images of the cross-fault velocity contrast and continuity of the fault plane along strike. The method has been applied to major fault systems around the world (e.g., Ben-Zion and Marlin 1991; Hough et al. 1994; McGuire and Ben-Zion 2005; Lewis et al. 2007; Zhao and Peng 2008; Zhao et al. 2010; Share and Ben-Zion 2016, 2018; Li and Peng 2016). In complement to FZHW analysis, teleseismic P-wave delay time analysis using stations across a fault provides a broader context of velocity contrast across the fault, which can be used to validate the estimations from FZHW study (e.g., Ozakin et al. 2012).

In this study, we employ the FZHW and teleseismic P-wave delay time analyses to constrain velocity contrasts across the ZLF using data recorded by 14 broadband seismic stations around the fault. In the following sections, we first describe the detailed analysis procedures employed in this paper. Then, we identify and verify FZHWs based on stations along ZLF and use them to estimate velocity contrasts. We further compare the estimates with results of teleseismic P-wave delay time analysis for verification. Finally, we discuss the dynamic implications of the observed velocity contrasts.

Methods

Fault Zone Head Wave

FZHW arrives before the direct P-wave and recorded by the stations of the slow side of fault wall with a normal distance to the interface x smaller than the critical distance x_c (Ben-Zion 1989), which is defined as:

$$x<x_c=r\cdot\tan[\cos^{-1}(\alpha_2/\alpha_1)] \quad (1)$$

Here r is the distance that the FZHW travels along the fault interface. α_1 and α_2 are the average P-wave velocities of the fast and slow sides of the fault, respectively.

FZHWs differ from direct P waves in many characteristics, including amplitude, frequency, first motion polarity, time difference, and sharpness, and can be identified by exploiting these differences. Ross and Ben-Zion (2014) developed an automatic detection algorithm to identify FZHWs and direct P waves, including filtering, preprocessing, and initial phase picking by applying a short-term-average/long-term-average (STA/LTA) ratio function. Then the initial picks are refined by utilizing kurtosis and skewness detectors. The algorithm has been shown to perform well on both synthetic seismograms and real data from several major faults in the world.

Because the FZHWs refract along the fault interface and radiate from the fault to the receiver, in contrast to the direct P waves that propagate from the source to the station, the horizontal polarization direction is also an important feature to distinguish FZHWs from direct P waves. We follow Bulut et al. (2012) to analyze the polarization directions in moving time windows using displacement data of the two horizontal components. In general, the signal-to-noise ratio (SNR) of horizontal records is lower than that of vertical records. For a time window, we compute the covariance matrix of the two horizontal components:

$$\mathbf{S}=\frac{\mathbf{XX}^{\mathrm{T}}}{N}=\begin{bmatrix} S_{\mathrm{nn}} & S_{\mathrm{ne}} \\ S_{\mathrm{ne}} & S_{\mathrm{ee}} \end{bmatrix} \quad (2)$$

Here $\mathbf{X}=[\mathbf{N}, \mathbf{E}]$, N is the length of the time window, and S indicate correlation of two component recordings. N, E represent displacement vectors of the two horizontal components. The eigenvalues (λ_1, λ_2) and eigenvectors ($\mathbf{u}_1$, $\mathbf{u}_2$) of the covariance matrix give the amplitudes and directions of the axes of the polarization ellipse (Jurkevics 1988). Assuming $|\lambda_1|\geq|\lambda_2|$, the polarization direction of the incoming P-wave, Az, is the azimuth of major eigenvector ($\mathbf{u_1}$) corresponding to the larger eigenvalue λ_1:

$$Az = \tan^{-1}\left(\frac{u_{11}}{u_{12}}\right) \tag{3}$$

Here u_{11} and u_{12} are the direction cosines of eigenvector $\mathbf{u_1}$.

We first employ the automatic detection algorithm of Ross and Ben-Zion (2014) to select candidates of FZHWs and direct P and further use the polarization direction analysis to confirm the phase identification. The refined FZHWs and direct P waves are finally used in moveout analysis to constrain P-wave velocity contrast across the ZLF. The differential arrival times between the FZHWs and direct P waves Δt are expected to increase with propagating distance r along the fault interface:

$$\Delta t \sim r\left(\frac{1}{\alpha_2} - \frac{1}{\alpha_1}\right) \sim r\left(\frac{\Delta\alpha}{\alpha^2}\right) \tag{4}$$

Here α and $\Delta\alpha$ are the average and absolute difference (contrast) of the P-wave velocity of the two fault sides (Ben-Zion and Malin 1991).

Teleseismic P-wave delay time analysis

Teleseismic P-wave samples the crustal structure with a near vertical incidence angle; hence, arrival time delays of the teleseismic P waves between two closely located stations across a fault from same earthquakes are often used to infer the velocity contrast between two fault sides (e.g., Ozakin et al. 2012; Qin et al. 2018, 2021; Qiu et al. 2017, 2021; Share et al. 2017, 2019). For the l-th teleseismic event, we first compute P-wave time residual at the i-th station, $\delta t_{l,i} = t^{o}_{l,i} - t^{c}_{l,i}$. Here $t^{o}_{l,i}$ and $t^{c}_{l,i}$ represent observed and computed P-wave arrival time, respectively. We employ the software package Crazyseismic (Yu et al. 2017) to pick up the observed arrival time and to compute the theoretical arrival time using the AK135 velocity model (Kennett et al. 1995). We then select the k-th station pair consisting of two closely located stations (i, j) across the fault to compute the P-wave delay time of the l-th event:

$$\Delta t_{k,\,l}(i, j) = \delta t_{l,\,i} - \delta t_{l,\,j} \tag{5}$$

Here we refer station j as the reference station and station i the target station. The final delay time of the pair is computed from the average of all recorded events:

$$\Delta \tilde{t}_k = \frac{1}{n}\sum_{l=1}^{n} \Delta t_{k,\,l}(i, j). \tag{6}$$

As mentioned above, if the first Fresnel zone of the two teleseismic raypaths overlap in the mantle, then the delay time reflects velocity difference of the crust between the two stations. In principle, this difference should be independent of source location, i.e., $\Delta t_{k,\,l}(i, j)$ measured from different teleseismic events are expected to show a little variation. Therefore, the standard deviation of $\Delta t_{k,\,l}(i, j)$ can be considered as the quality control of the measured delay time for each station pair.

If elevation and Moho depth across the fault vary greatly, P-wave traveltime difference arising from those factors should also be considered. The net teleseismic P-wave delay time caused by velocity contrast at the k-th station pair is given by

$$\Delta t_k^{'} = \Delta \tilde{t}_k - \Delta \tilde{\tau}_k - \Delta T_k \tag{7}$$

Here $\Delta \tilde{\tau}_k$ and ΔT_k represent the arrival time differences resulting from the differences of elevations and Moho depth. We assume that the teleseismic P-wave arrives at a near vertical incident angle, the arrival time difference due to elevation difference of the k-th station pair $\Delta \tilde{\tau}_k$ is given by

$$\Delta \tilde{\tau}_k = \Delta d_k / \alpha_0 \tag{8}$$

Here Δd_k is the elevation difference between the two stations of the k-th pair and α_0 is the P-wave velocity of the upper crust. Assuming the Moho beneath the target station of the k-th pair is Δh_k deeper than that of the reference station, then the delay time correction associated with Moho depth, ΔT_k, can be written as:

$$\Delta T_k = \frac{\Delta h_k}{\alpha_c \cos(\theta_c)} - \frac{\Delta h_k}{\alpha_m \cos(\theta_m)} \tag{9}$$

Here α_c and α_m are the P-wave velocity of the lowermost crust and uppermost mantle. θ_c and θ_m are the corresponding angles of the P-wave raypath segments.

Once effects of topographic elevation and Moho depth are corrected, $\Delta t_k^{'}$ can be used to compute P-wave velocity contrast across the fault (Ozakin et al. 2012):

$$\frac{\delta\alpha}{\alpha} = -\frac{\Delta t_k^{'} \cdot \alpha \cdot \cos(\theta)}{h} \tag{10}$$

Here α and $\delta\alpha$ are the average and absolute difference (contrast) of the P-wave velocity of the two stations across the fault. h and θ are the reference crustal thickness and the average incident angle of the teleseismic P waves, respectively.

Data and Results

To monitor seismic activity along the ZLF after the 2014 M_w 6.1 Ludian earthquake, the Institute of Earthquake Forecasting, China Earthquake Administration (CEA) deployed a temporary seismic network in the area. The instruments were a mixture of Nano Trilllum-120, Guralp CMG-3T and 40T. We picked 13 stations of different deployment periods from the temporary array and one station (ZAT) from the permanent regional seismic network. The 13 stations include 3 groups: (1) L08, L13, L14 and L16 have been running since January 2016; (2) J03, A04, and A05 were operating between January 2016 and December 2019; (3) Y07, Y09, Y10, Y11, Y14 and T28 were newly installed in January 2020. 15576 local events were detected from

January 2016 to July 2018. We selected 2968 events that have a fault normal distance less than 13 km for FZHW analysis. Hypocentral locations of all the 2968 events were determined with a 3-D traveltime table in Chuandian area, and 2076 events were relocated by HypoDD (Waldhauser and Ellsworth 2000).

As ZLF is a complicated fault zone system that comprises three secondary faults, we select earthquakes occurred within a 13 km-wide rectangle parallel to the surface trace of the main fault approximated by a straight line. The preprocessing steps of data include removal of linear trend and mean from each seismogram, and bandpass filtering with a 0.5-20 Hz Butterworth filter. We then apply the automatic identification and picking algorithm (Ross and Ben-Zion 2014) to detect candidates of FZHWs. To improve identification, we also inspect the automatic results manually. Some candidate phases with amplitudes similar to the noise level prior to P waves are discarded. After this initial quality control, the candidate FZHWs identified at ZAT, L08, J03, A05 and A04 are 299, 204, 164, 134, and 85 respectively (Figure S1 for ZAT station, available in the electronic supplement).

To examine and refine the initial detection of the FZHW arrivals of the candidate events, we follow Bulut et al. (2012) to perform particle motion analysis on the FZHWs and direct P-wave arrivals. The initial time differences between FZHWs and direct P-wave arrivals are used as window lengths, and 4 windows forward and 4 windows backward are set to the waveforms centered at the direct P arrivals. The azimuth of horizontal particle motion trajectories at each window and eigenvalue ratio between two successive windows are calculated by equations (2) and (3) and are marked on the top of each window shown in Figure 2. If the eigenvalue ratios in FZHW window and the first P arrival window are both much larger than those in the preceding noise windows, and the particle motion trajectories of the two windows are approximately fault-normal and source-receiver back azimuth, respectively, we label the emergent early arrival as FZHW. The FZHW and direct P arrivals are refined according to the particle motion trajectories in the two corresponding windows. If only the eigenvalue ratio in the first P arrival window is large, and the particle motion of the phase points to the source-receiver direction, we consider the early arrival as a misdetection and reject it. Figure 2 displays an example of horizontal particle motions of different windows measured at ZAT. ZAT is located at the southeast side of the ZLF fault (Figure 1), the polarization direction of FZHW and P arrival windows changes from oblique to parallel to source-receiver direction (Figure 2).

We find robust detection of FZHWs at four stations, ZAT, L08, J03 and A04, and the number of detections is 18, 14, 9, and 12 events, respectively. Here stations ZAT and L08 are in the northeastern segment of ZLF while stations J03 and A04 are in the SW segment of the ZLF. To estimate the velocity contrast across the fault, we apply the moveout analysis to FZHWs that perform well in the horizontal particle motion analysis. This is done by aligning all the seismograms with FZHWs at each station along the refined initial times of the direct P waves (red dots), respectively (Figure 3). We find two types of time-distance moveout of FZHW with respect to the direct P wave from two clusters of earthquakes (hereafter cluster #1 and cluster #2). The first type of FZHW shows a linear moveout that increases with the along-fault distance (i.e., larger moveout for longer distance). Such FZHWs are usually associated with a deep fault interface that separates two crustal blocks with distinctive velocity structures, as illustrated in Figure 3e. In particular, the FZHWs are from earthquakes located within 30 km from ZAT (Figure 3a) and 50 km from L08 (Figure 3b). The second type of FZHW shows a constant moveout (~0.13 s) independent to the along-fault distance. This is seen from events with far-offsets recorded by ZAT

(> 30 km in Figure 3a), L08 (> 50 km in Figure 3b), and all events recorded by stations J03 and A04 (Figures 3c-d).

Events from cluster #1 are distributed in the central and NE section of the ZLF and events from cluster #2 are in the aftershock zone of the Ludian M_w 6.1 earthquake (Figure 4). Furthermore, both ZAT and L08 are situated at the southeast side of the ZLF fault, and stations in the other side, such as L16 (Figure 1), show no FZHW arrivals prior to P (Figure 5). These observations suggest that in the northeastern segment of the ZLF P-wave velocity in the southeast block is slower than that in the northwest side.

In the southwestern segment of the fault, the FZHWs events recorded by the two stations, J03 and A04, belong to cluster #2 in the aftershock zone of the Ludian earthquake. However, J03 and A04 are not located at the same side of the ZLF fault, suggesting this segment of the fault has more complicated structure. As we discuss in the next section, we speculate that the FZHWs are likely refracted arrivals traveling along the two sides of a local low velocity aftershock region rather than propagating through the fault interface.

Equation (4) suggests that the differential times between FZHWs and direct P waves increase linearly with along fault propagating distance. We first apply a linear regression to obtain the slope of the time-distance moveout slop, and then assume a constant P-wave velocity of the study area, 6.06 km/s, based on the tomographic study of Li et al. (2019), to compute the cross-fault velocity contrast. For station ZAT and L08 in the NE section of ZLF, the corresponding velocity contrasts related to cluster #1 are 2.3%, 2.5%, respectively. The observed velocity contrasts are at the low end across major fault systems estimated from previous studies (e.g., ~3.4% for North Anatolian fault in Najdahmadi et al., 2016; ~2.8% in Share et al. 2016 for San Andreas fault). Najdahmadi et al., (2016) attribute the ~3.4% low velocity contrast in the Karadere segment of the north

Anatolian fault in Turkey to the small offset of Karadere fault. The ZLF in this study consists of several secondary faults and thus may have small amount of offset.

In the SW segment of the fault, we observed the second types of FZHWs from earthquakes in the the aftershock zone of the Ludian earthquake at J03 and A04. We noticed that J03 and A04 are located at both side of the ZLF fault, suggesting that this segment of the fault has more complicated structure. As we discuss in the next section, we speculate that the FZHWs are likely refracted arrivals traveling along the two sides of a local low velocity aftershock region rather than propagating through the fault interface (Figure 3f).

In addition to the above four stations, we find two types of additional arrivals besides the direct P waves at station A05 (Figures S2). The first group show early arrivals before the direct P waves and have all of characteristics of FZHWs including a fault-normal polarization direction. The second group are characterized by a reversed order of particle motion directions, namely, the particle motion of the early phase approximately points to source-receiver direction and the second phase approximately points to fault direction (Figure S3). The probable reason for this complication is that both the first and second arrivals may comprise the direct P and FZHW waves.

To further confirm the velocity contrasts derived from FZHWs, we conduct the delay time analysis (Ozakin et al. 2012) using teleseismic P waves recorded by pairs of stations sitting across the ZLF. We extract P waves of 11 teleseismic events from continuous recordings of the vertical components based on the PDE catalog (https://earthquake.usgs.gov/earthquakes/, Table 1). The 11 earthquakes occurred between January 2020 and December 2020 and are recorded by station groups (1) and (3). They are distributed in the distance range of 60° to 90° and have a magnitude greater than 5.5 (Figure 1).

We first remove the linear trend and means from each waveform and apply a bandpass filter of 0.1-5.0 Hz. We select 6 station pairs across the fault, which are located at different section of the ZLF. To estimate the P-wave arrival time delays, we first obtained the estimated arrival times using the AK135 model. We then pick the nearest maximum peaks of the direct P-wave as the observed arrival times in a [-5 s, 5 s] time window. The waveforms are aligned by the observed direct P picks to estimate the time delays (Figure 6). For each event, we calculate the residual times δt_i at each station and the delay times $\Delta t_{k,l}(i,j)$ of each station pair. For each station pair, we average $\Delta t_{k,l}(i,j)$ over the available events to obtain the final delay time measurements $\Delta\tilde{t}_k$. We employ α_0=5.56 km/s (Zuo et al. 2019) in calculating the elevation related arrival time correction $\Delta\tilde{\tau}_k$ using equation (8) (Table 2). We employ the Moho depth map derived from H-κ stacking of receiver functions recorded at 35 stations in the study area (Wang et al. 2015). The estimated Moho depth beneath each station is listed in Table 3 and is used computing the Moho depth correction ΔT_k. We employ equation (9) and use α_c=6.5 km/s, α_m=8.04 km/s, θ_c=24°, and θ_m=30° in computing ΔT_k. The velocities are taken from AK135 model (Kennett et al. 1995) and the incident angle are computed based on an epicentral distance of 60° and a source depth of 0 km. The calculated ΔT_k are also shown in Table 2.

After correcting the delay times related to station elevation and Moho depth, we obtain the net teleseismic P-wave delay times of 6 station pairs, which are listed in Table. The station pair ZAT-L16 located at the NE segment shows a delay time as large as 0.75 s, indicating that the P-wave velocity in the block by the southeast side is prominently smaller than that by the northwest side. The rest 5 pairs located in the SW segment exhibit a much smaller P-wave delay time, varying from 0.01 s to 0.20 s, suggesting velocity contras across the SW segment is less significant.

Since ZLF is a boundary between two tectonic blocks, therefore we assume that the cross-fault velocity contrast is persistent across the entire crust. We further assume that the crust beneath the study area has an average Moho depth of 46 km and P-wave velocity α=6.5 km/s. Using an incident angle θ=24° (i.e., equivalent to an epicentral distance of 60° and a source depth of 0 km), we obtain a P-wave traveltime of 7.75 s in the crust. The velocity contrasts converted from teleseismic P-wave delay times are in the range of 0.1-9.6% (Table 2). The NE station pair ZAT-L16 has a contrast of ~9.6%, much larger than the ~2.5% estimated from FZHW data. The large discrepancy between FZHW and P-wave delay time data observed in the NE segment is likely related to their spatial sensitivity. It is worth noting that the velocity contrast calculated from FZHWs analysis is the velocity difference of the two fault sides at seismogenic depth averaged over along-fault propagation distance, whereas the velocity difference estimated from the teleseismic P-wave delay time represent the distinction of crust column below the two stations. It reflects not only velocity contrast between the two sides of the fault but also lateral heterogeneities inside the two blocks. In addition, the contrast given by teleseismic P wave delay time is also affected by the accuracy of corrections for topography and Moho depth variation, which are much less reliable than estimations from FZHWs. Therefore, we only use the polarity of the velocity contrast derived from the teleseismic delay time analysis when we compare the results of the two datasets.

Figure 7 summarizes the velocity contrasts estimated from FZHWs and teleseismic P-wave delay time analysis. For comparison, we also showed lateral variations of density at 12 km obtained by Chen et al. (2014). In the NE segment, both FZHWs and teleseismic P-wave delay times indicate Vp of the southeast side of the fault has a slightly lower than that of the northwest side. In the SW section, the teleseismic P-wave delay time analysis indicates much smaller lateral variations. Here, FZHWs are observed at stations in both side of the fault, suggesting that the

FZHWs are generated at the edge of a localized low velocity zone instead of a bi-material fault interface. In general, the lateral velocity variations observed here agree with changes in density.

Discussions

Correlation of Ludian aftershock sequence and FZHWs

The classical FZHWs generated by a bi-material interface of major faults are only recorded by the stations at the slower block. However, there is another type of the FZHWs, which are generated by the edges of a localized low velocity zone or basin, can be recorded the stations at both sides (Li et al. 2016; Najdahmadi et al. 2016; Yang et al. 2015). This type of FZHWs usually has a constant moveout regardless of the along-fault distance. In this study, it is observed at far-offset records of stations ZAT (> 30 km in Figure 3a) and L08 (> 50 km in Figure 3b), as well as the records of J03 and A04 (Figures 3c-d) (cluster #2).

Different from previous studies, we interpret these FZHWs (with almost constant moveout pattern) as head waves refracted along the aftershock zone of the 2014 Ludian Mw 6.1 earthquake, rather than attributing them to edge refraction of a local low velocity zone right beneath the stations (Najdahmadi et al. 2016, Figure 12a; Qiu et al., 2017). This is because almost all the events generating this type o FZHWs (cluster #2) are restricted in the aftershock area of the Ludian M_w 6.1 (Figure 4). Relocation of the aftershock sequence of the Ludian M_w 6.1 (Fang et al. 2014; Wang et al. 2014) with the double-difference method indicates that aftershocks are distributed in two predominant directions, SE direction and SW direction, which form a conjugate or inverse L shape. Magnetotelluric study (Cai et al. 2017) shows a high electrical conductivity anomaly at depths shallower than 8 km that overlaps with the inverse L shape aftershock region. The low electrical conductivity of the surrounding rocks might suggest that they are mechanically strong which prevents the Ludian earthquake from rupturing through them. At ~12 km depth, the aftershock region also appears to be a localized low-density zone based on a gravity study (Chen et al. 2014, Figure 7). Riaz et al. (2017) conducted a double-difference tomographic inversion. They interpreted the aftershock area of Ludian Mw 6.1 with low Vp and low Poisson's ratio as a compositional anomaly with high quartz contents, and the surrounding area with high Poisson' ratio as granitic rocks and/or metamorphic rocks. Therefore, the cluster #2 earthquakes are concentrated in a volume with high electrical conductivity, low density, and low seismic velocity, suggesting the volume either has high volatile concentration or slightly different composition with a sharp boundary that allows for the propagation of head waves.

Dynamic implication from the velocity contrasts

In the northeastern section of the ZLF, velocity contrasts across the fault estimated from the FZHW analysis at ZAT and L08 using cluster #1 earthquakes are 2.3% and 2.5%, respectively. The net teleseismic P-wave delay time between station pair ZAT-L16 derived from teleseismic P-wave delay time analysis is 0.65 s. Both suggests that P-wave velocity by the southeast side, i.e., the South China block (Figure 1), is significantly slower than that by the northwest side in the northeastern section of the ZLF. In the southwestern section of the ZLF, the net teleseismic P-wave delay time from teleseismic P-wave arrival analysis indicate that P-wave velocity has a little change from the northwest side block and the southeast side block (Table2, e.g., net teleseismic P-wave delay time between station pairs L13-L14, Y10-Y14 and Y10-Y11). This is supported by the density model at 12 km depth from gravity inversion of Chen et al. (2014) (Figure 7). In the NE section of ZLF, the southeast side has slower velocity and lower density, while in the SW section of ZLF, both sides have faster velocity and higher density.

In the NE section of ZLF, the Cenozoic sedimentary Zhaotong basin (ZTB) is located by the southeast side of ZLF and Sayuhe secondary fault (Chang et al. 2014). The basin is dominated by the ZLF, and thus extends to NE strike (Wang 2010) (Figure 1). This region is an important brown coal producing area in Yunnan Province. The basins evolved through three periods: rapid fault depression period in early Pliocene, stable depression period in late Pliocene and stable expansion period in early Pleistocene. From the double difference seismic tomographic result at Zhaotong region (Wang et al. 2014b), ZTB shows a large range of low velocity anomaly down to 10 km depth. The Yiliang region, which is also located by the south side of ZLF in the NE section, are the central part of the sedimentary cover area in SCB, and the lithology of the upper layer is mainly composed of Jurassic and Cretaceous sand shale (Lu et al. 2009). The lithology of the upper crust in the southeast side block of ZLF in the NE section would explain the low velocity anomaly relative to that in the northwest side block.

The significant difference in seismic velocity structure between the NE and SW parts of the ZLF fault could have significant implication on seismogenesis along the fault. Slip along a planar bi-material interface generates asymmetric dynamic stress field at the tips of ruptures propagating in the opposite along-strike directions (Weertman 1980; Ampuero and Ben-Zion 2008). For sub-shear ruptures, at the tip propagating in the direction of slip on the compliant solid, there is dynamic reduction of frictional strength; while in the opposite direction, there is dynamic increase of strength (Ben-Zion 2001; Ampuero and Ben-Zion 2008). Accordingly, for a typical sub-shear rupture, the statistically preferred rupture direction is expected to be the slip direction of the slower block (compliant block). In the NE section of right-lateral strike-slip ZLF, since the southeast side is the slower block, the relative motion of the slower block is to the SW direction. This means that the preferred rupture propagation direction of a future earthquake in the NE section is from northeast to southwest. Compared with the contrast elastic properties across the fault in the NE section, the similar medium property across the fault in the SW section suggests the asymmetric dynamic stress field will not be produced, thus the slip might be cut off by the central to SW section. This implies that a large earthquake nucleating in the NE section of ZLF would hardly propagate through the SW section.

If we assume that an earthquake nucleating in the northeast end of ZLF, and propagate along the fault to the central section (e.g., Ludian County), the maximum surface rupture length would be about 82 km. According to the magnitude-rupture length empirical formula (Leonard 2010), for intraplate strike-slip earthquakes, the moment magnitude M_w can be empirically calculated:

$$M_w = 1.52 \log_{10} L\_SR + 4.33 \tag{11}$$

Here L_SR is the surface rupture length (82 km), and the maximum magnitude is about M_w 7.2.

Conclusions

We present two datasets and analyses to constrain velocity structure along the ZLF. Firstly, moveouts of FZHWs relative to the direct P waves are used to estimate velocity contrasts across the fault at seismogenic depth. In the NE section, only two stations, ZAT and L08, located at the southeast side of the fault, show robust FZHWs, leading to estimates of cross-fault velocity differences varying from 2.3% to 2.5%. In the SW section, the events generating non-moveout FZHWs are concentrated in the aftershock zone of the 2014 Mw 6.1 Ludian earthquake, and FZHWs are recorded by stations at both sides of the fault. Analysis of P-wave delay times of paired stations from 11 teleseismic events confirms that velocity contrast across the fault is significant in the NE section and is less clear in the SW segment. Combining the observations from both analyses and other geophysical studies, we conclude that there is a distinct different between NE and SW segments of the ZLF. In the NE segment, the P-wave velocity of the South China block in the southeast side is prominently slower than that of Daliangshan sub-block in the northwest side. The FZHWs observed in the southwest are refracted head waves propagating along the edges of a localized low velocity zone that overlaps with aftershock region of M_w 6.1 Ludian earthquake. We suggest that lithological difference across the fault in the NE section can be attributed for the prominent velocity contrast. The velocity contrast also indicates that earthquakes nucleating in the NE section of ZLF would hardly propagate through the SW section. Consequently, the corresponding maximum magnitude calculated from the magnitude-rupture length empirical formula is approximately M_w 7.2, significantly lower than a hypothetic rupture that runs across the entire ~150-km long ZLF.

Data and sources

The seismic data recorded by stations from the temporary seismic network and permanent regional seismic network are provided by the Institute of Earthquake Forecasting, China Earthquake Administration (CEA) and cannot released to the public. The teleseismic events are based on the PDE catalog (https://earthquake.usgs.gov/earthquakes/,last accessed October 2021, Table 1). The Ludian M_w 6.1 aftershock sequences are obtained from Li et al. (2019). The focal mechanism of Ludian M_w 6.1 earthquake are obtained from the global CMT web page (https://www.globalcmt.org/, last accessed July 2021). All of the figures were produced by using the GMT software of Wessel & Smith (1998). The preliminary results for station ZAT after the application of automatic picking algorithm and the examples of two sets of events identified at station A05 can be seen in the electronic supplement to this article.

Acknowledgments

This study was jointly supported by supported by the National Key R&D Program of China (2017YFC1500303), the Specialized Research Program of the Institute of Earthquake Forecasting, China Earthquake Administration under the title "The dense observation and seismicity trace analysis in the downstream reservoir areas of Jinsha River" (Grant No. 2020IEF0708), and

"Velocity contrast study across the Xiaojiang Fault from the analysis of Fault Zone Head Waves" (Grant No. 2021IEF0502). The waveform data for this study were provided by the Institute of Earthquake Forecasting, China Earthquake Administration. The automatic identification and picking algorithm were developed by Ross and Ben-Zion (2014). The seismic data preprocessing software package Crazyseismic was developed by Yu et al. (2017).

We are also grateful for the constructive comments and suggestions from the two anonymous reviewers, which significantly improved the quality of this paper.

References

Allam, A. A., Y. Ben-zion, Z. Peng (2014). Seismic imaging of a biomaterial interface along the Hayward fault, CA, with fault zone head waves and direct P arrivals, *Pure Appl. Geophys.* **171**(11), 2993-3011.

Ampuero, J. P., and Y. Ben-Zion (2008). Cracks, pulses, and macroscopic asymmetry of dynamic rupture on a bimaterial interface with velocity-weakening friction, *Geophys. J. Int.* **173**(2), 674-692. https://doi.org/10.1111/j.1365- 246X.2008.03736.x.

Andrews, D. J., and Y. Ben-Zion (1997). Wrinkle-like slip pulse on a fault between different materials, *J. Geophys. Res.*, https://doi.org/10.1029/96jb02856.

Bennington, N. L., C. Thurber, Z. Peng, H. Zhang, and P. Zhao (2013). Incorporating fault zone head wave and direct wave secondary arrival times into seismic tomography: Application at Parkfield, California, *J. Geophys. Res.* **118**(3), 1008-1014.

Ben-Zion Y (1989). The response of two joined quarter spaces to SH line sources located at the material discontinuity interface, *Geophys. J. Int.* **98**(2), 213-222.

Ben-Zion Y., Malin P (1991). San Andreas fault zone head waves near Parkfield, California, *Science* **251**(5001), 1592-1594.

Ben-Zion, Y (2001). Dynamic rupture in recent models of earthquake faults, *J. Mech. Phys. Solids* **49**, 2209-2244.

Bulut, F., Y. Ben-Zion, and M. Bohnhoff (2012). Evidence for a biomaterial interface along the Mudurnu segment of the North Anatolian Fault Zone from polarization analysis of P waves, *Earth Planet Sci. Lett.* 327-328, 17-22.

Cai, J., X. Chen, X. Xu, J. Tang, L. Wang, C. Guo, B. Han, Z. Dong (2017). Rupture mechanism and seismotectonics of the M_s 6.5 Ludian earthquake inferred from three-dimensional magnetotelluric imaging, *Geophys. Res. Lett.* **44**, 1275-1285.

Chang Z., R. Zhou, X. An, Y. Chen, Q. Zhou, J. Li (2014). Late-quaternary activity of the Zhaotong-Ludian fault zone and its tectonic implication, *Seisology and Geology* (in Chinese) **36**(4), 1260-1276.

Chen S., Q. Wang, Q. Wang, Y. Wang, H. Lu, W. Xu, L. Shi, and F. Guo (2014). The 3D density structure and gravity change of Ludian M_s 6.5 Yunnan epicenter and surrounding regions, *Chinese J. Geophys.* (in Chinese) **57**(9), 3080-3090.

Crotwell, H. P., T. J. Owens, and J. Ritsema (1999). The TauP Toolkit: Flexible seismic travel-time and ray-path utilities, *Seismol. Res. Lett.* **70**, 154-160.

Fang, L., J.Wu, W. Wang, Z. Lv, C. Wang, T. Yang, and S. Zhong (2014). Relocation of the aftershock sequence of the M_s 6.5 Ludian earthquake and its seismogenic structure, *Seismology and Geology* (in Chinese) **36**(4), 1173-1185.

Guo, B., Q. Liu, J. Chen, L. Liu, and S. Qi (2009). Teleseismic P-wave tomography of the crust and upper mantle in Longmenshan area, west Sichuan, *Chinese J. Geophy.* (in Chinese) **52**(2), 346-355.

Hough, S. E., Y. Ben-Zion, and P. Leary (1994). Fault zone waves observed at the southern Joshua Tree earthquake rupture zone, *Bull. Seismol. Soc. Am.* **84**(3), 761-767.

Huang, Z., L. Wang, M. Xu, and D. Zhao (2018). P wave anisotropic tomography of the SE Tibetan Plateau: Evidence for the crustal and upper-mantle deformations. *J. Geophys. Res.* **123**, 8957-8978.

Leonard, M. (2010). Earthquake fault scaling: self-consistent relating of rupture length, width, average displacement, and moment release. *Bull. Seismol. Soc. Am.* **100**(5A), 1971-1988.

Lewis, M. A., Y. Ben-Zion, and J. McGuire (2007). Imaging the deep structure of the San Andreas Fault south of Hollister with joint analysis of fault zone head and direct P arrivals, *Geophys. J. Int.* **169**(3), 1028-1042.

Li Z., and Z. Peng (2016). Automatic identification of fault zone head waves and direct P waves and its application in the Parkfield section of the San Andreas Fault, *Geophys. J. Int.* **205**(3), 1326-1341.

Li D., Z. Ding, P. Wu, M. Li, and Q. Gu (2019). Deep structure of the Zhaotong and Lianfeng fault zones in the eastern segment of the Sichuan-Yunnan border and the 2014 Ludian M_s 6.5 earthquake, *Chinese J. Geophys.* (in Chinese) **62**(12), 4571-4587.

Lv, Y., G. Li, G. Zhang, J. Cai, R. Ji, and W. Wang (2009). Characteristics of the geological hazard distribution and the control measures in Yiliang county, Yunnan. *Carsologica Sinica* (in Chinese) **28**(2), 219-224.

McGuire, J., and Y. Ben-Zion (2005). High-resolution imaging of the Bear Valley section of the San Andreas fault at seismogenic depths with fault-zone head waves and relocated seismicity, *Geophys. J. Int.* **163**(1), 152-164.

Najdahmadi, B., M. Bohnhoff, and Y. Ben-Zion (2016). Bi-material interfaces at the Karadere segment of the North Anatolian Fault, northwestern Turkey, *J. Geophys. Res.* **121**(2), 931-950.

Ozakin, Y., Y. Ben-Zion, M. Aktar, H. Karabulut, and Z. Peng (2012). Velocity contrast across the 1944 rupture zone of the North Anatolian fault east of Ismetpasa from analysis of teleseismic arrivals, *Geophys. Res. Lett.* **39**(L08307), 1-6.

Qin, L., Y. Ben-Zion, H. Qiu, P-E. Share, Z. E. Ross, and F. L. Vernon (2018). Internal structure of the san Jacinto fault zone in the trifurcation area southeast of Anza, California, from data of dense seismic arrays. *Geophys. J. Int.* **213**(1), 98-114. https://doi.org/10.1093/gji/ggx540.

Qin, L., P-E. Share, H. Qiu, A. A. Allam, and Y. Ben-Zion (2021). Internal structure of the San Jacinto fault zone at the Ramona Reservation, north of Anza, California, from dense array seismic data, *Geophys. J. Int.* **224**(2), 1225-1241.

Qiu, H., Y. Ben-Zion, and Z. E Ross (2017). Internal structure of the San Jacinto fault zone at Jackass Flat from data recorded by a dense linear array, *Geophys. J. Int.* **209**(3), 1369-1388.

Qiu, H., Y. Ben-Zion, R. Cachings, M. R. Goldman, and J. Steidl. Seismic imaging of the M_w 7.1 Ridgecrest earthquake rupture zone from data recorded by dense linear arrays. *J. Geophys. Res.* **126**(7), https://doi.org/10.1029/2021JB022043.

Riaz, M. S., Y. Zheng, and X. Xiong (2017). Refined 3D seismic-velocity structures and seismogenic environment of the M_s 6.5 Ludian earthquake, *Bull. Seism. Soc. Am.* **107**(6), 3023-3036.

Ross, Z. E., and Y. Ben-Zion (2014). Automatic picking of direct P, S seismic phases and fault zone head waves, *Geophys. J. Int.* **199**, 368-381.

Share, P. E., and Y. Ben-Zion (2016). Bi-material interfaces in the South San Andreas fault with opposite velocity contrasts NW and SE from San Gorgonio Pass, *Geophys. Res. Lett.* **43**(20), 10680-10687.

Share, P. E., Y. Ben-Zion, Z. E. Ross, H. Qiu, and F. L. Vernon (2017). Internal structure of the San Jacinto fault zone at Blackburn Saddle from seismic data of a linear array. *Geophys. J. Int.* **210**(2), 819-832.

Share, P. E., and Y. Ben-Zion (2018). A biomaterial interface along the northern San Jacinto fault through Cajon Pass, *Geophys. Res. Lett.* **45**(21), 11622-11631.

Share, P. E., A. A. Allam, Y. Ben-Zion, F. Lin, and F. L. Vernon (2019). Structural Properties of the San Jacinto Fault Zone at Blackburn Saddle from Seismic Data of a Dense Linear Array. *Pure Appl. Geophys.* **176**(3), 1169-1191.

Shlomai, H., and J. Fineberg (2016). The structure of slip-pulses and supersheer ruptures driving slip in bimaterial friction. *Nature Communications*, https://doi.org/10.1038/ncomms11787.

Waldhauser, F. and W. L. Ellsworth (2000). A double-difference earthquake location algorithm: Method and application to the northern Hayward Fault， California, *Bull. Seismol. Soc. Am.* **90**, 1353-1368.

Wang, Z., D. Zhao, and J. Wang (2010). Deep structure and seismogenesis of the north‐south seismic zone in southwest China, *J. Geophys. Res*. **115**(B12334), 1-19.

Wang, J. (2010). Preliminary evaluation on exploration prospect of CBM resources of the Neogene lignite in zhaotong basin. *China Coalbed Methane* (in Chinese) **7**(2), 3-6.

Wang, W., J. Wu, L. Fang., and G. Lai (2014a). Double difference location of the Ludian M_s 6.5 earthquake sequences in Yunnan province in 2014, *Chinese J. Geophys*. (in Chinese) **57**(9), 3042-3051.

Wang X., X. Yu, and W. Zhang (2014b). Seismic tomography at Zhaotong region and analysis of seismotectonic in Yiliang area. *Progress in Geophy*. (in Chinese) **29**(49), 1573-1580.

Wang, X., Z. Ding, Y. Wu, and L. Zhu (2015). The crustal structure and seismogenic environment in the Ludian M_s 6.5 earthquake region, *Chinese J. Geophys.* (in Chinese) **58**(11), 4031-4040.

Weertman, J. (1980). Unstable slippage across a fault that separates elastic media of different elastic constants. *Geophys. J. Int.* 85(B3), 1455-1461. https://doi.org/10.1029/JB085iB03p01455.

Wei, W., Z. Jiang, D. Shao, Z. Shao, X. Liu, Z. Zou, and Y. Wang (2018). Coseismic displacements from GPS and inversion analysis for 2014 Ludian 6.5 earthquake. *Chinese J. Geophys.* (in Chinese) **61**(4), 1258-1265.

Wells, D. L., and K. L. Coppersmith (1994). New empirical relationships among magnitude, rupture width, rupture area, and surface displacement, *Bull. Seism. Soc. Am.* **84**(4), 974-1002.

Wen, X, D. Fang, G. Yi, F. Long, and L. Qi (2013). Earthquake potential of the Zhaotong and Lianfeng fault zones of the eastern Sichuan-Yunnan border region, *Chinese J. Geophys.* (in Chinese) **56**(10), 3361-3372.

Wessel, P., and W. H. F. Smith (1998). New, Improved Version of Generic Mapping Tools Released, *Eos* **79**(47), 579.

Xu X., G. Jiang., G. Yu, X. Wu, and X. Li (2014). Discussion on seismogenic fault of the Ludian M_s 6.5 earthquake and its tectonic attribution, *Chinese J. Geophys.* (in Chinese) **57**(9), 3060-3068.

Xu, X., Z. Ding, and F. Zhang (2015). The teleseismic tomography study by P-wave traveltime data beneath the southern South-north Seismic Zone, *Chinese J. Geophys.* (in Chinese) **58**(11), 4041-4051.

Yang, T., J. Wu, L. Fang, and W. Wang (2014). Complex structure beneath the southeastern Tibetan Plateau from teleseismic P-wave tomography, *Bull. Seismol. Soc. Am.* **104**(3), 1056-1069.

Yang, W., Z. Peng, B. Wang, Z. Li, and S. Yuan (2015). Velocity contrast along the rupture zone of the 2010 M_w 6.9 Yushu, China, earthquake from fault zone head waves, *Earth Planet Sci. Lett.* **416**, 91-97.

Yang, W., B. Wang, Z. Peng, X. Tian, and S. Yuan (2020). The structure feature if step-over basin along Garze-Yushu fault from analysis of fault zone head wave, *Chinese J. Geophys.* (in Chinese) **63**(3), 1197-1213.

Yu, C., Y. Zheng, and X. Shang (2007). Crazyseismic: a MATLAB GUI-based software package for passive seismic data preprocessing, *Seismological Research Letters* **88**, 410-415.

Zhao, P., and Z. Peng (2008). Velocity contrast along the Calaveras fault from analysis of fault zone head waves generated by repeating earthquakes, *Geophys. Res. Lett.* **35**(1), L01303.

Zhao, P., Z. Peng, Z. Shi, M. A. Lewis, and Y, Ben-Zion (2010). Variations of the Velocity contrast and rupture properties of M6 earthquakes along the Parkfield section of the San Andreas Fault. *Geophys. J. Int.* **180**(2), 765-780.

Zheng, X., C. Zhao, S. Zheng, and L. Zhou (2019). Crustal and upper mantle structure beneath the SE Tibetan Plateau from joint inversion of multiple types of seismic data. *Geophys. J. Int.* **217**, 331-345.

Zuo, K., C. Zhao, and C. Zhao (2019). 3D Vp, Vs, and Vp/Vs structures of reservoirs area in the lower reaches of Jinsha rive, China, Annual Meeting of Chinese Geoscience Union.

Full mailing address for each author

Xian Zheng: Institute of Earthquake Forecasting, China Earthquake Administration, Beijing, 100036, China

Cuiping Zhao: Institute of Earthquake Forecasting, China Earthquake Administration, Beijing, 100036, China

Hongrui Qiu: now at Earth, Atmospheric and Planetary Sciences, Massachusetts Institute of Technology, Cambridge, MA02139, USA, also at Department of Earth, Environmental and Planetary Sciences, Rice Universitys, Houston,TX77005, USA

Fenglin Niu: Department of Earth, Environmental and Planetary Sciences, Rice Universitys, Houston, TX77005, USA

Ce Zhao: Institute of Geophysics, China Earthquake Administration, Beijing, 100081, China

Table 1. The information of 11 events selected for the calculation of velocity contrasts in Figure 7.

Date (mm/dd/yy)	Time (hh:mm)	Lat.(°)	Lon. (°)	Mw	Δ[¶] (deg.)	φ[§] (°)
03/18/20	03:13	-13.136	167.028	6.1	73.46	114.58
04/08/20	10:02	-15.719	-177.549	5.5	87.56	108.92
05/12/20	22:41	-12.067	166.649	6.6	72.56	113.87
06/06/20	10:55	-16.725	177.346	5.7	83.80	112.24
06/10/20	07:55	-17.427	-178.916	5.6	87.24	111.05
07/21/20	20:56	-20.805	-178.633	6.0	89.13	113.84
08/04/20	16:31	12.562	166.615	5.6	72.81	114.32
09/12/20	02:37	-17.880	-178.005	5.6	88.22	111.02
10/06/20	10:11	-17.996	-178.472	5.9	87.89	111.33
10/30/20	11:10	-8.820	161.041	5.5	66.19	114.34
11/03/20	08:18	-19.989	-177.464	5.7	89.69	112.60

Table 2. The arrival time differences and the corresponding velocity contrasts of each station pair after the elevation modification.

Station pairs	$\Delta\tilde{t}$ (s)	$\Delta\tilde{\tau}$ (s)	ΔT (s)	$\Delta t'$ (s)	Std (s)	$-\delta\alpha/\alpha$ (%)
ZAT-L16	0.57	-0.083	-0.092	0.75	0.08	9.6
L13-L14	0.05	0.005	-0.047	0.09	0.10	1.2
Y10-Y14	0.08	-0.042	-0.006	0.13	0.10	1.7
Y10-Y11	0.19	0.063	-0.009	0.14	0.08	1.8
Y07-Y09	0.23	0.016	0.010	0.20	0.06	2.6
Y07-T28	-0.05	-0.070	0.014	0.01	0.08	0.1

$\Delta\tilde{t}$: delay time measurement; $\Delta\tilde{\tau}$: elevation correction; ΔT: Moho depth correction; $\Delta t'$: net delay time

Table 3. The crustal thickness at each station interpolated from Wang et al. (2015).

Station	Lat (°)	Lon (°)	Ele (km)	Moho depth (km)
ZAT	27.3	103.7	1.92	45.96
L08	27.5	104.0	1.76	45.76
L16	27.3	103.4	2.39	49.80
L13	27.0	103.6	1.99	47.22
L14	27.1	103.4	1.96	49.16
Y10	26.8	103.3	2.38	51.19
Y14	27.0	103.2	2.61	51.46
Y11	26.8	103.1	2.02	51.55
Y07	26.5	103.0	2.09	52.54
Y09	26.7	103.0	2.00	52.13
T28	26.5	102.8	2.48	51.95

List of Figure Captions

Figure 1. A map of the study area centered on the Zhaotong-Ludian Fault (ZLF).

Figure 2. Horizontal particle motion analysis at station ZAT for the event in Figure 1 (green dot).

Figure 3. The velocity seismograms of station ZAT (a), station L08 (b), station J03 (c) and station A04 (d) after the application of automatic picking algorithm and the horizontal particle motion analysis.

Figure 4. Map-views and cross-sections of the events selected after the particle motion analysis for station ZAT (a), L08 (b), J03 (c), and A04 (d).

Figure 5. The velocity seismograms of the same events at station ZAT (a) and station L16 (b).

Figure 6. The example waveforms from the teleseismic event shown in Figure 1 (green dots in left top insert).

Figure 7. The summary map of inferences determined from FZHW analysis and teleseismic P-wave delay time analysis.

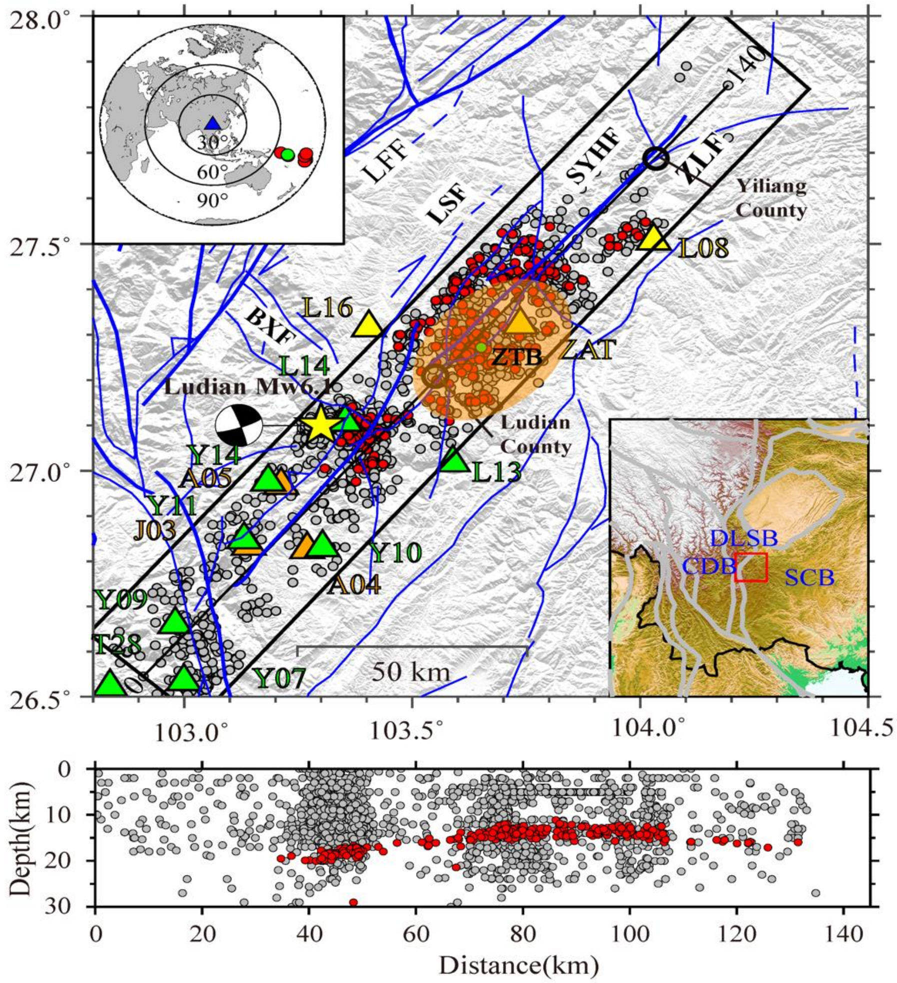

Figure 1. A map of the study area centered on the Zhaotong-Ludian Fault (ZLF). The grey dots, red dots and green dot represent the locations of 2968 local events recorded from January 2016 to July 2018 within 13 km normal distance to the fault, the candidate FZHWs and the event used in Figure 2. The epicenter of the 2014 Ludian M_w 6.1 earthquake is marked as red star. The solid blue lines denote the faults in this region. The yellow triangles, orange triangles, green triangles represent stations used for both FZHWs analysis and teleseismic P-wave delay time analysis, FZHWs analysis only, teleseismic P-wave delay time analysis only, respectively. The orange translucent ellipse denotes the Zhaotong basin (ZTB). The capital letters in the white boxes are the abbreviations for the faults; ZLF: Zhaotong-Ludian Fault; LLF: Lianfeng Fault; LSF: Longshu

Secondary Fault; SYHF: Sayuhe Secondary Fault; BXF: Baogunao-Xiaohe Secondary Fault. The red dots and green dots in the left top inset represent the location of the 11 teleseismic events for teleseismic P-wave delay time analysis and the example events in Figure 6, respectively. The blue triangle shows the location of the study area. The right bottom inset shows the tectonic framework of SE Tibetan and South China block (SCB). Lower panel shows the cross section view along the ZLF.

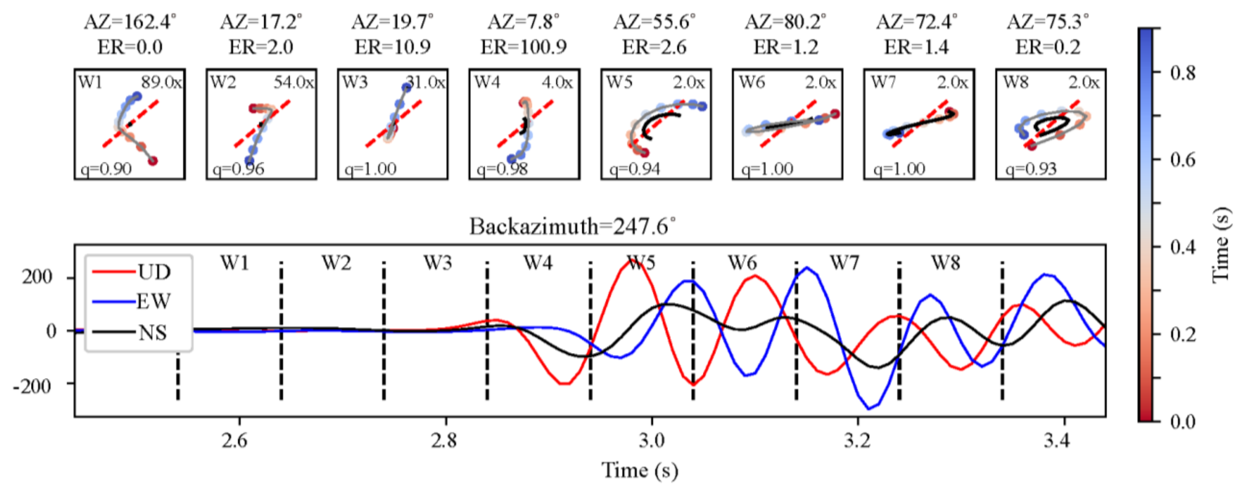

Figure 2. Horizontal particle motion analysis at station ZAT for the event in Figure 1 (green dot). The red dash lines in the top panels indicate the back azimuth of the reference event. The dash dot lines represent the trajectory of horizontal particle motion in each time window and are color coded according to the time sequence. The trajectory of each window is magnified with the amplification factor marked at the top right of the panel. In the bottom panel, the displacement seismograms of the vertical and two horizontal components are marked in red, blue and black lines, respectively.

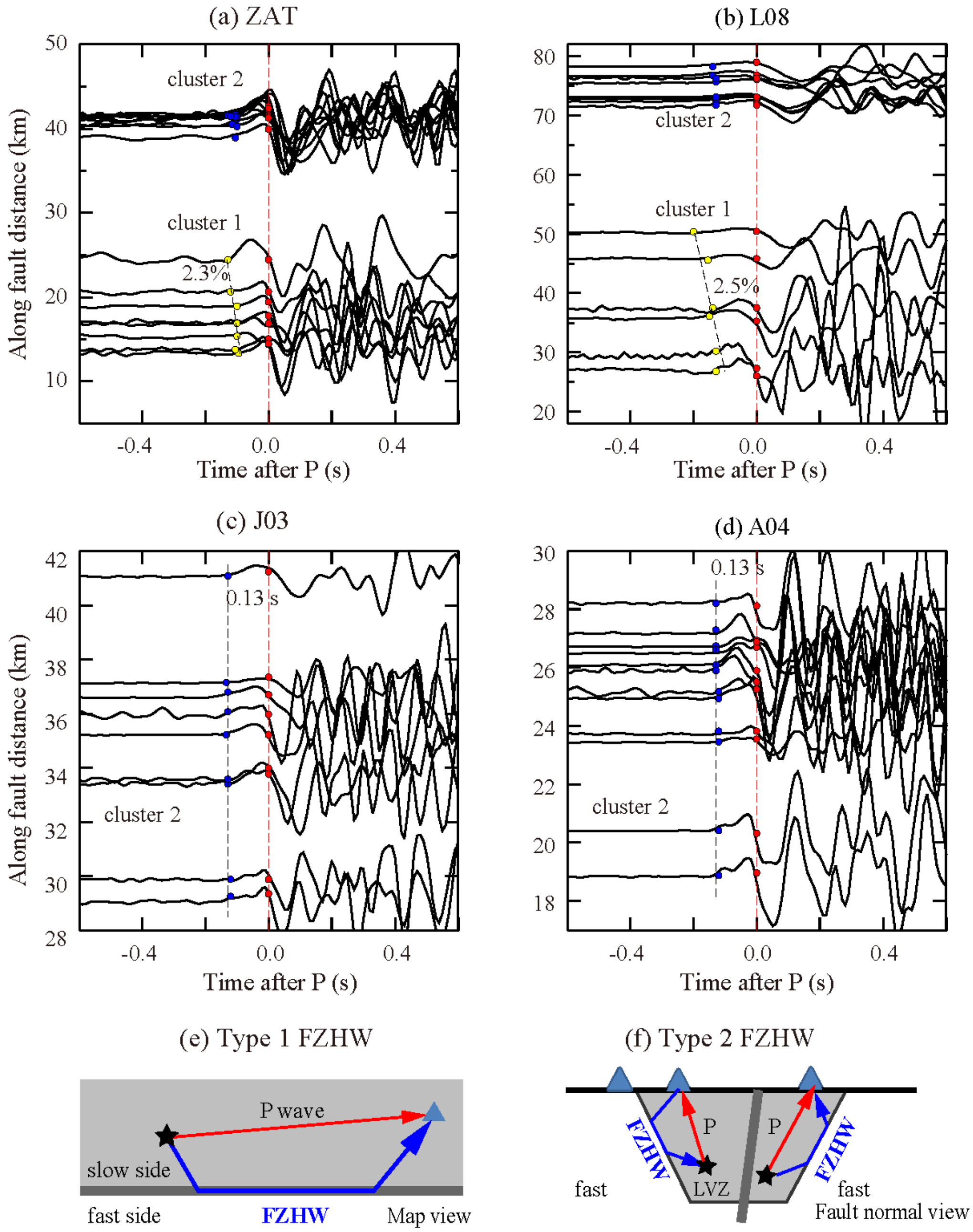

Figure 3. The velocity seismograms of station ZAT (a), station L08 (b), station J03 (c) and station A04 (d) after the application of automatic picking algorithm and the horizontal particle motion analysis. The waveforms are aligned on the direct P arrivals (red dots) and are plotted with along fault distance. The yellow dots and blue dots mark the refined FZHW arrivals from cluster #1 and

cluster #2, respectively. The red dash lines and the black dash lines show the onset of the direct P wave and the least squares fitting of the data with the slope, respectively. (e) and (f) are the schematic diagrams showing the raypaths of the type 1 and type 2 FZHWs.

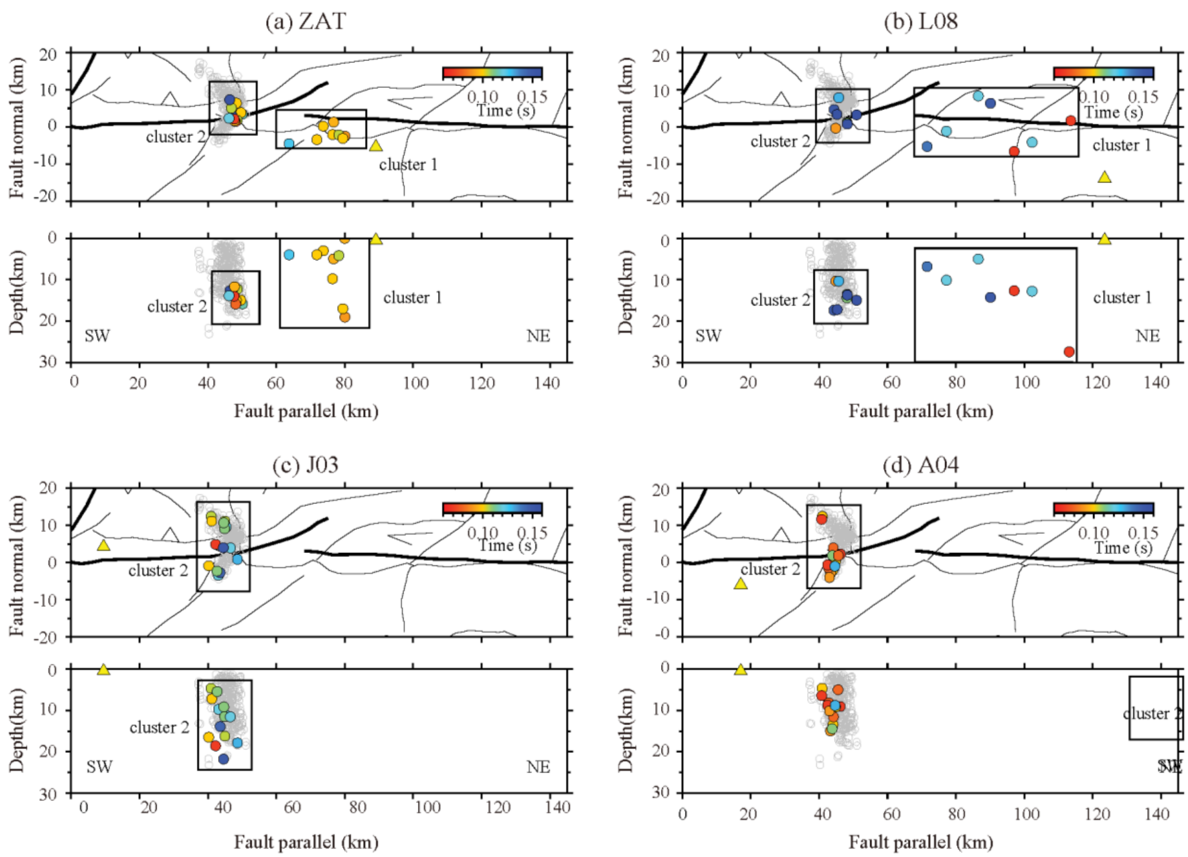

Figure 4. Map-views and cross-sections of the events selected after the particle motion analysis for station ZAT (a), L08 (b), J03 (c), and A04 (d). The solid circles denote the epicenters of the events and are color coded according to the moveouts between the FZHW and the direct P-wave. The grey hollow circles represent the epicenter of the Ludian M_w 6.1 aftershock sequences (Li et al., 2019). The yellow triangles mark the locations of the station for analysis.

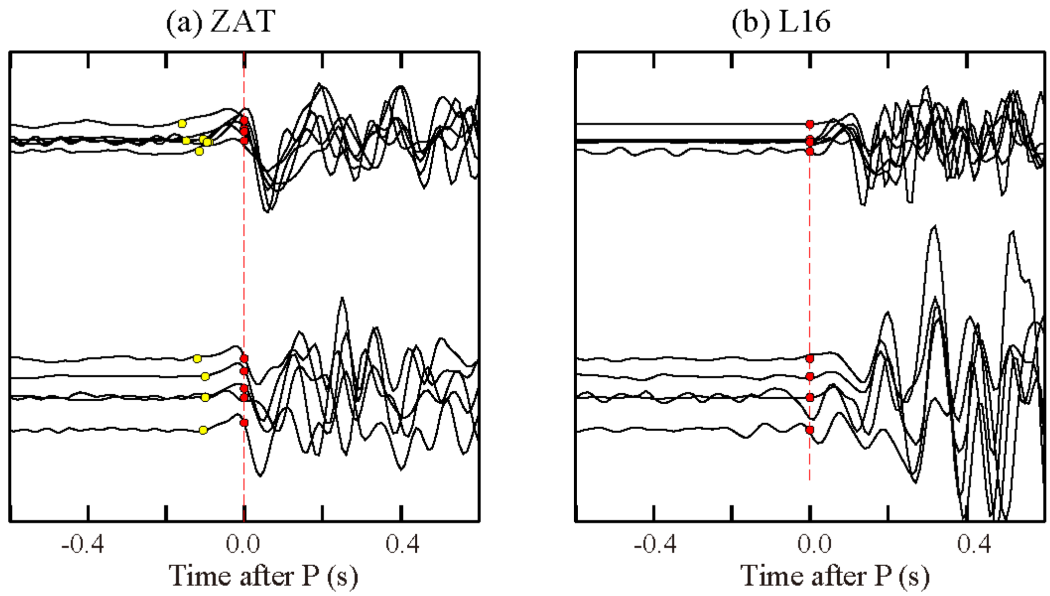

Figure 5. The velocity seismograms of the same events at station ZAT (a) and station L16 (b). The red dots and yellow dots represent the direct P picks and FZHW picks, respectively.

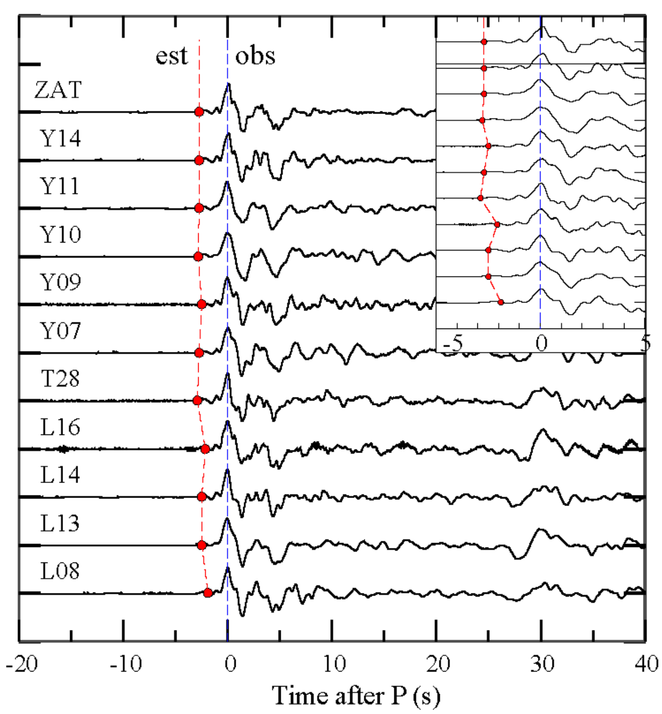

Figure 6. The example waveforms from the teleseismic event shown in Figure 1 (green dots in left top insert). The red dots denote the estimated time calculated by the AK135 model and the blue dash line marks the maximum peaks of the direct P-wave. The right top insert is the zoom-in plot for the traces in [-5 5]s time window. The event information: original time: 2020-05-12 22:41 ;latitude: -12.06°; longitude:166.649°; magnitude: M_W:6.6 (Table 1).

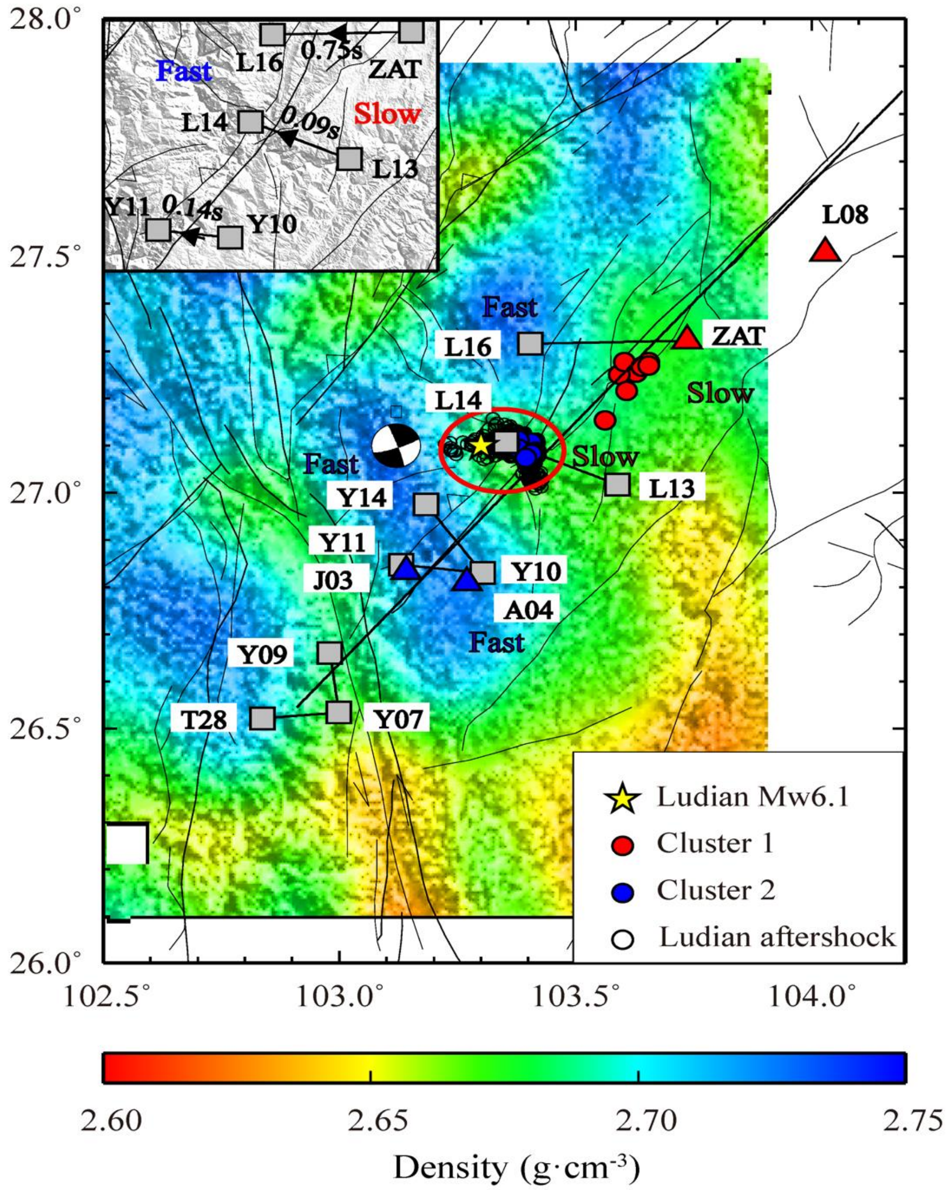

Figure 7. The summary map of inferences determined from FZHW analysis and teleseismic P-wave delay time analysis. The main features are overlain on the densities at 12 km depth from gravity inversion of Chen et al. (2014). The red circles and blue circles represent events generating FZHWs from cluster #1 and cluster #2, respectively; and the red triangles and blue triangles denote the corresponding stations that identify them. The grey squares and black lines between them represent station pairs used for teleseismic P-wave delay time analysis (Table 2). The yellow star

and black hollow circles represent the epicenter of the Ludian M_w 6.1 mainshock and aftershock sequences (Li et al., 2019), respectively. The left top insert is the zoom-in plot of the net teleseismic P-wave delay time between three station pairs (ZAT-L16, L13-L14,Y10-Y11). The black arrows point from the slower block to faster block. The corresponding delay times between the station pairs are marked above the arrows. In the northeastern section of ZLF, the SE side has slower velocity and lower density, while in the southwestern section of ZLF, both sides have faster velocity and higher density. The Ludian M_w 6.1 aftershock area marked by the red hollow circle is a localized low velocity and density zone.

Supplementary materials

List of Supplemental Figure Captions

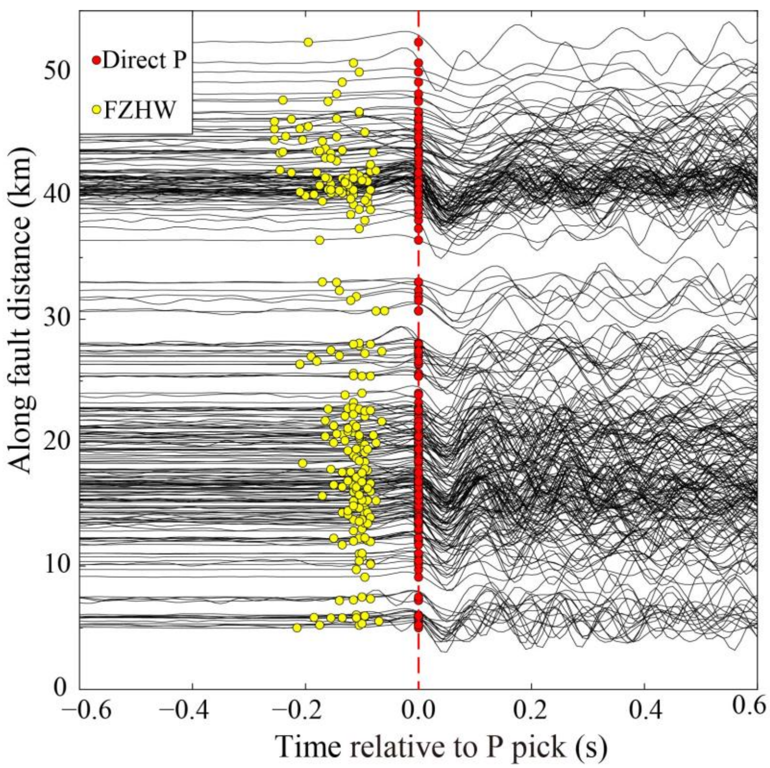

S1. The preliminary results for station ZAT after the application of automatic picking algorithm. The waveforms are aligned on the direct P arrivals (red dots) and are plotted with along fault distance. The yellow dots mark the automatic FZHW picks. Epicenters of these events are shown in Figure 1 (red circles).

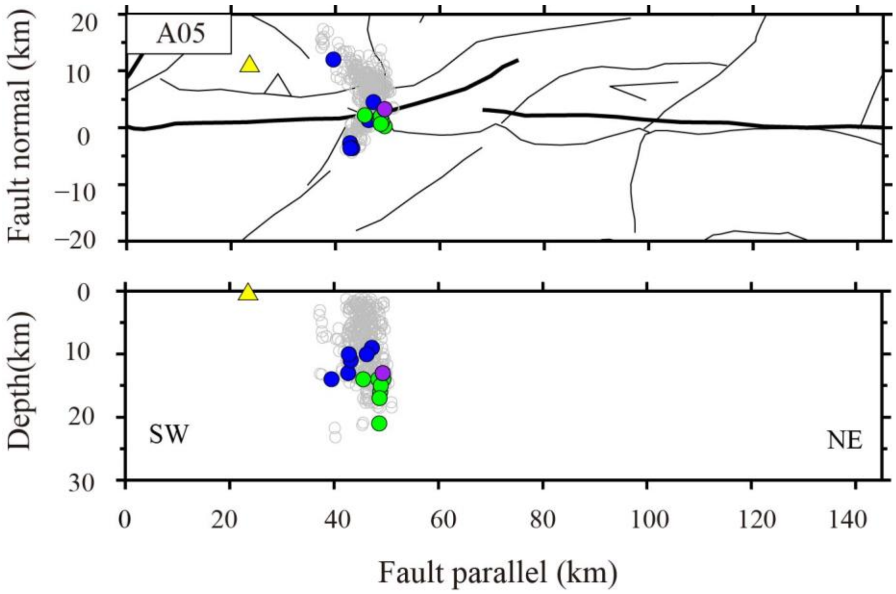

S2. The map-views and cross-sections of the two sets of events identified at station A05. The blue solid circles, green solid circles, and grey hollow circles indicate the epicenter of the events generating FZHWs and FZRWs, and the Ludian M_w 6.1 earthquake aftershock sequences (Li et al. 2019). The purple solid circle marks the epicenter of the event used in S3.

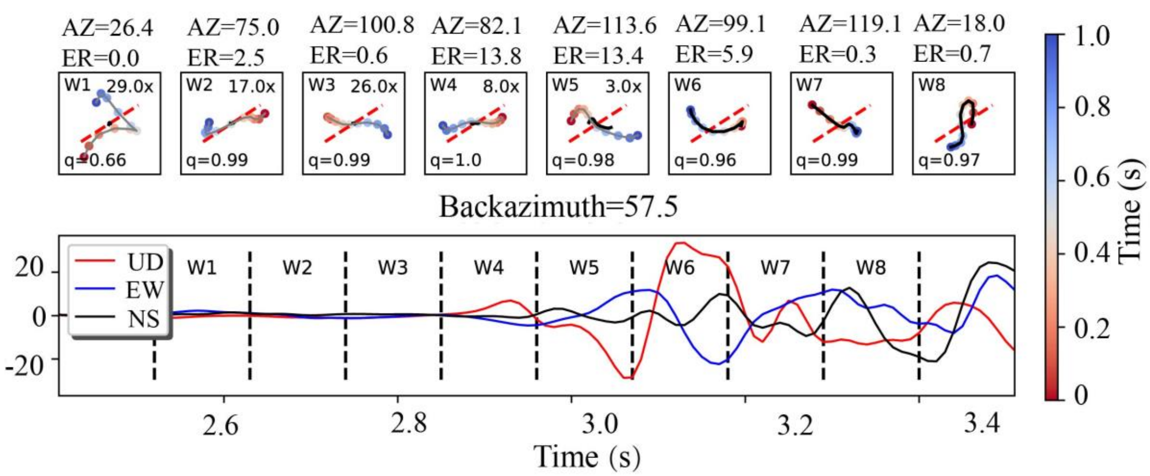

S3. Horizontal particle motion analysis at station A05 for the event in figure S2 (purple circle). The symbols have the same meaning as those in figure 3.